CMOS MEMS Thermoelectric Infrared Sensor With Plasmonic Metamaterial Absorber for Selective Wavelength Absorption and Responsivity Enhancement

Pen-Sheng Lin, Ting-Wei Shen, Kai-Chieh Chan, and Weileun Fang, *Fellow, IEEE*

***Abstract*—This study demonstrates the integration of thermoelectric type MEMS infrared (IR) sensor with plasmonic metamaterial absorber (PMA) through a standard CMOS process platform to improve the responsivity of MEMS IR sensor in a specific range of wavelength. Based on an existing thermoelectric IR sensor with the serpentine film structure, the proposed device further combines with a Metal-Insulator-Metal (MIM) type PMA. The absorber consists of a top antenna layer, a middle dielectric spacer, and a bottom reflector, and the metal and dielectric films in the standard CMOS process are exploited in this study to implement the MIM design. The advantage of narrow linewidth in CMOS process can meet the need of critical dimensions for MIM antennas. The absorption wavelength can be adjusted by varying the pattern and dimension of antennas. The MIM PMAs are designed in the coupling regime, and hence the shifting of absorbed wavelength caused by the variation of antenna dimensions from fabrication can be prevented. The feasibility of the presented MIM PMA is demonstrated by simulations and experiments. The absorption spectra measured by FTIR show the capability of proposed MIM PMAs in extending the absorption range of far-infrared. Measurement results also indicate that under the same sensor footprint and the equal number of thermocouples, the device integrated with the proposed MIM PMA has a 20 percent improvement in responsivity as well as detectivity.**

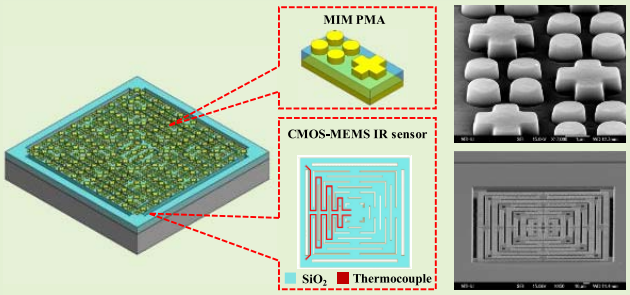

***Index Terms*—CMOS-MEMS, infrared sensor, metamaterial, metal-insulator-metal, thermoelectric.**

I. Introduction

THE micro-electro-mechanical-system (MEMS) technology has been exploited to implement the chip scale IR sensors. Presently, MEMS IR sensors have been widely applied to human motion detection, gas sensing, non-contact temperature measurement, night vision, etc. The IR sensors sensitive to specific ranges of wavelengths are required for different applications. For example, the wavelength range for human motion detection is usually in the far-infrared region because of the high transmission rate in the atmosphere [1]. For the application of gas sensing, the wavelength range depends on the molecules of target gases, which is usually in the Near-IR and the Mid-IR regions [2]. In general, the sensing mechanism of MEMS IR sensors is based on heat transfer, so that incident radiation of different wavelengths can be absorbed and detected [3]. Therefore, additional filters are required for the MEMS IR sensor to select the wavelength. It is straightforward to assemble filters onto sensing chips through packaging, for example the TO-can package [4]. However, the assembling approach may sacrifice the advantages of batch fabrication for MEMS IR sensors. Moreover, the device size will be increased, and the extra cost is needed to prepare different kinds of filters. The approach to add filters through the wafer level chip-scale package (WLCSP) [5] could reduce the assembly cost and also shrink the die size, yet the transmission rate of filter is limited by the material of capped wafer.

Integrating absorbers directly on MEMS IR sensors is another promising approach to achieve the wavelength selection or enhance the absorptivity through wafer-scale processes [6]–[14]. Various techniques such as, microstructure

Manuscript received April 27, 2020; accepted May 21, 2020. Date of publication May 25, 2020; date of current version September 3, 2020. This work was supported by the Ministry of Science and Technology (MOST), Taiwan, under Grant MOST 108-2218-E-007-034. The associate editor coordinating the review of this article and approving it for publication was Dr. Joseph Shor. *(Corresponding author: Weileun Fang.)*

The authors are with the Department of Power Mechanical Engineering, National Tsing Hua University, Hsinchu 300, Taiwan, and also with the Institute of NanoEngineering and MicroSystems, National Tsing Hua University, Hsinchu 300, Taiwan (e-mail: fang@pme.nthu.edu.tw).

Digital Object Identifier 10.1109/JSEN.2020.2997534

type [6]–[9], dielectric thin film type [10], [11], and porous material type [12]–[14], have been reported to implement and integrate absorbers with MEMS IR sensor. Among these techniques, microstructure absorbers rely on the principle of interference or metamaterials to absorb thermal radiation [15], [16]. The absorbed wavelength can be properly selected by changing the dimensions of microstructure (such as the thickness of Fabry-Pérot-like absorber [15] or the in-plane dimension of Metal-Insulator-Metal (MIM) absorber [16]). In this regard, the process requirements for small linewidth patterning and uniformity are needed. Moreover, dielectric thin film absorbers are composed of dipolar molecule materials such as SiO_2 and Si_3N_4 whose polarization losses occur within the range of microwave to far-infrared [17]. The absorption which occurs in the oscillation wavelength of these dipolar molecules could be employed to select the required wavelength of incoming light. Such absorber is compatible with the CMOS process but the absorption spectrum is restricted by available materials. Another concern is that the dielectric film will increase the response time of MEMS IR sensors [2]. Porous material absorbers utilize materials with high surface roughness such as gold black and platinum black to improve the absorptivity. However, the porous material has a wide absorption spectrum with poor wavelength selectivity. Among these existing approaches, microstructure absorbers exhibit the advantages to select the absorption wavelength through microfabrication processes with no special materials required.

This study presents the concept to integrate the microstructure absorber (MIM type plasmonic metamaterial absorber (PMA)) with the MEMS IR sensor to improve its responsivity in the far-infrared region. The MIM PMA consists of a top antenna layer, a middle dielectric spacer, and a bottom reflector, and its absorption wavelength can be tuned by regulating the dimensions of antenna. Since the in-plane dimensions of antenna should be in sub-wavelength, the process requirements such as the small linewidth and thin film thickness uniformity are critical to precisely define the features of MIM PMAs. Moreover, the process integration of MIM PMA with MEMS IR sensors is also not straightforward. Thus, this study extends the approach in [18] to adopt the existing CMOS process to implement the present device. The standard CMOS processes are mature and also available in commercial foundries. In addition, the stacking of multiple layers including metal and dielectric films and the capability of defining extremely small linewidth of existing CMOS processes [19] are especially suitable to realize MIM PMAs. In this study, the integration of MIM PMAs with MEMS thermoelectric IR sensors is designed and implemented by using the standard CMOS process. Measurement results show that the presented MIM PMA designs could enhance the absorptivity, achieve wavelength selection, and extend the absorption range of the MEMS IR sensor as well.

II. Principle and Design Considerations

Based on the standard 0.18μm 1P6M (one poly and six metal layers) CMOS process offered by the commercial foundry (Taiwan Semiconductor Manufacturing Company Ltd., or named TSMC), the proposed IR sensor with MIM PMA is designed and implemented in this study. Thus, the available materials and the stacking of thin films are limited by the standard CMOS process. In this section, the design considerations of the proposed sensor will be introduced first and then various designs of the MIM PMA will be discussed. The performances of different MIM PMA designs are predicted and investigated by the simulations.

A. Sensor Design

Based on the Seebeck effect, MEMS thermoelectric IR sensors can convert a temperature difference, ΔT, between hot and cold regions of a thermopile, into an open circuit voltage difference, ΔV. This effect can be expressed as,

$$\Delta V = \alpha_s \Delta T, \tag{1}$$

where α_s is the Seebeck coefficient of the thermopile. In addition, if the MEMS thermoelectric IR sensors are expressed with a RC equivalent mode (where R_{th} and C_{th} stand for thermal resistance and thermal capacitance respectively), and then the temperature difference ΔT in the state of thermal equilibrium (i.e. $dC_{th}/dt = 0$) is [20],

$$\Delta T = R_{th} \alpha \Delta \phi, \tag{2}$$

where α is the absorptivity of sensors and $\Delta\phi$ is the variation of incident radiation power. Furthermore, to indicate the capability of sensors regarding converting radiation power into output voltage, the responsivity R_s is introduced and defined by,

$$R_s = \frac{\Delta V}{\Delta \phi}. \tag{3}$$

By substituting Eq. (1) and Eq. (2) into Eq. (3), the responsivity can be expressed as,

$$R_s = \alpha \alpha_s R_{th}. \tag{4}$$

According to Eq. (4), the responsivity of MEMS thermoelectric IR sensors is proportional to three factors including the absorptivity, the Seebeck coefficient, and the thermal resistance. Thus, this study presents the design to integrate the MIM PMA with the MEMS structure. By varying the design of MIM PMA, the absorptivity in the targeted wavelength range can be improved and further enhance the responsivity of IR sensor.

Figure 1 shows the schematic illustration of the proposed IR sensor. This study exploits the available materials for the standard CMOS process to design the proposed device. As the isometric view displayed in Fig. 1a, the proposed IR sensor consists of the SiO_2 (the dielectric layers of the CMOS process) suspended structure with embedded poly-Si thermocouples. Moreover, two metal layers of the CMOS process are used to form the MIM PMA on top of the SiO_2 suspended structure. The zoom-in illustration further shows the candidate shape designs of the MIM PMA. Another inset depicts the suspended structure with embedded thermocouples. The thermocouple is designed to have a serpentine shape to lengthen the heat-transfer path under the same sensor footprint [21], and then improve the temperature difference.

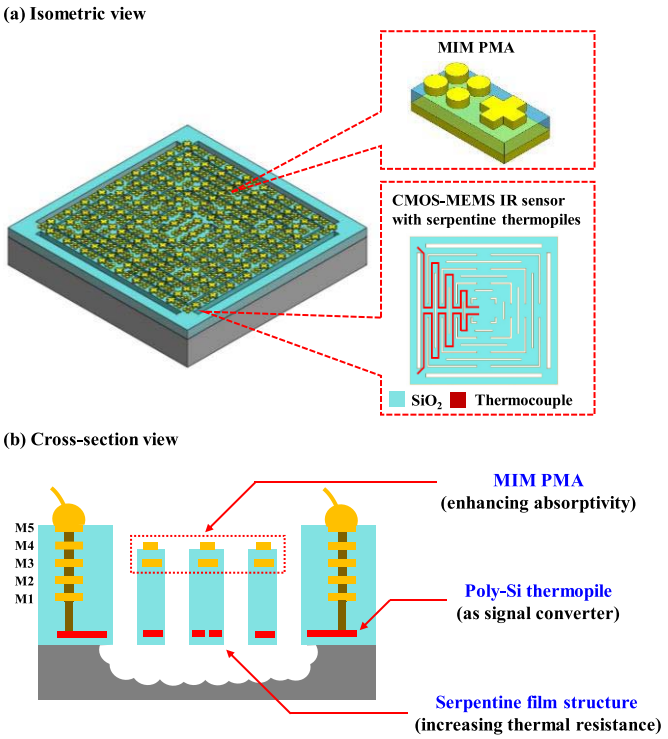

Fig. 1. The schematic illustration of proposed MEMS IR sensor integrated with MIM PMA, (a) the isometric view, and (b) the cross-section view.

In addition, there are total eight pairs of thermocouples, and each pair consists of the N-type and P-type poly-Si. The stacking of metal, SiO_2, and poly-Si layers for the proposed device are displayed in the cross-section view of Fig. 1b. Note the metal films for MIM PMA are metal-3 (M3) and metal-4 (M4) layers of the CMOS process. The structure suspended on the substrate for thermal isolation is also observed.

B. MIM PMA Design

This study exploits the MIM PMA layers shown in Fig. 1 to enhance the performances of the MEMS IR sensor. As shown in Fig. 2a, the dielectric materials absorb incoming radiation through their innate electric dipoles, and especially, under the resonant frequency of electric dipole oscillation, the absorptivity will rise promptly [17]. Moreover, as indicated in Fig. 2b, when illuminated by irradiation in specific wavelength, the MIM PMA will produce oscillation of free electrons (also called plasmon) in the top antenna layer and the bottom reflector layer, and further lead an artificial electric dipole oscillation within the dielectric spacer [16]. The wavelength absorption of the middle dielectric layer caused by the oscillation of innate electric dipoles may couple with that of the MIM PMA resulted from the artificial electric dipole oscillation. This study exploits the SiO_2 film of CMOS process as the material of middle dielectric layer since the dielectric dispersion of SiO_2 film has an absorption peak (9.3μm) within the target far-infrared region [17]. The commercial finite element method (FEM) software is employed to predict the optical performance of MIM PMA. Based on the design rules of the standard 0.18μm 1P6M CMOS process, the wavelength

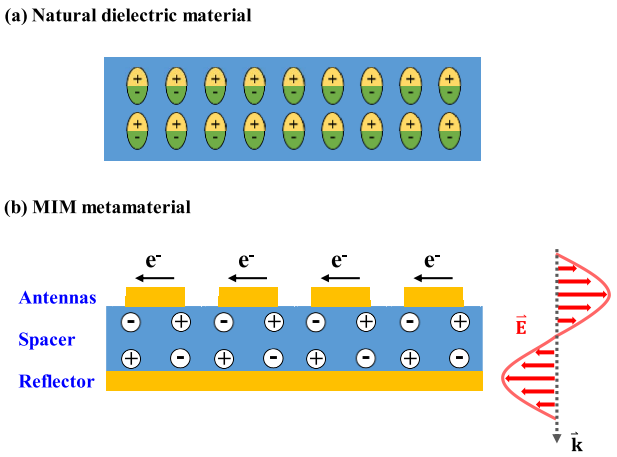

Fig. 2. The illustration of absorption mechanisms, (a) natural dielectric materials utilize electric dipole oscillations to absorb the incoming radiation, and (b) MIM PMAs produce electric dipoles induced by plasmons between top antennas and bottom reflector when illuminated by radiation.

absorption spectrum of MIM PMA when in the coupling or uncoupling regimes will be investigated and discussed.

In the uncoupling regime, the absorption peak wavelength, λ_{abs}, of MIM PMA can be determined by [22],

$$\lambda_{abs} = 2n(L_c+2\delta), \tag{5}$$

where n is the refractive index of dielectric spacer, δ is the evanescent extension of MIM antennas, and L_c is the characteristic length of MIM antennas (e.g. by using the two designs proposed in this study, as shown in Fig. 3a-b, for the cross-shape antenna, the L_c is the length L of cross; for the circle-shape antenna, L_c is the diameter D of circle). According to Eq. (5), the wavelength λ_{abs} can be modulated by the characteristic length L_c of MIM antenna. This study further investigates the variation of λ_{abs} with L_c by using the FEM software. Schematic illustrations in Fig. 3a-b display the two antenna designs in this study. The FEM simulation could predict the L_c of these two antenna designs so that the λ_{abs} of MIM PMA is close to the absorption wavelength of SiO_2. The L_c of cross-shape antenna ranges from $L = 1.5\mu$m to $L = 4.0\mu$m with 0.5μm interval and the width of cross-shape antenna W is fixed at 1μm; the L_c of circle-shape antenna ranges from $D = 1.5\mu$m to $D = 4.0\mu$m with 0.5μm interval. Note that the dielectric layer is SiO_2 film for the standard CMOS process, and its refractive index is assumed as a loss-less constant ($n = 1.44$) in the FEM model. Moreover, in the FEM model, a linear-polarized plane wave is normally incident to the MIM PMA. Figure 3c shows the typical simulation results of localized dipole resonance for a cross-shape antenna with $L = 2.5\mu$m. The distribution of electric-field intensity (color map) and electric dipole (arrows) in the MIM PMA model can be predicted. Simulation results in Fig. 4a-b respectively present the absorption spectra of cross-shape and circle-shape MIM PMAs with different characteristic length L_c (cross length L and circle diameter D), and Fig. 4c further depicts the variation of the absorption peak wavelength λ_{abs} with the cross length L and circle diameter D. It indicates the λ_{abs} increases with the L_c of antenna, such trend agrees

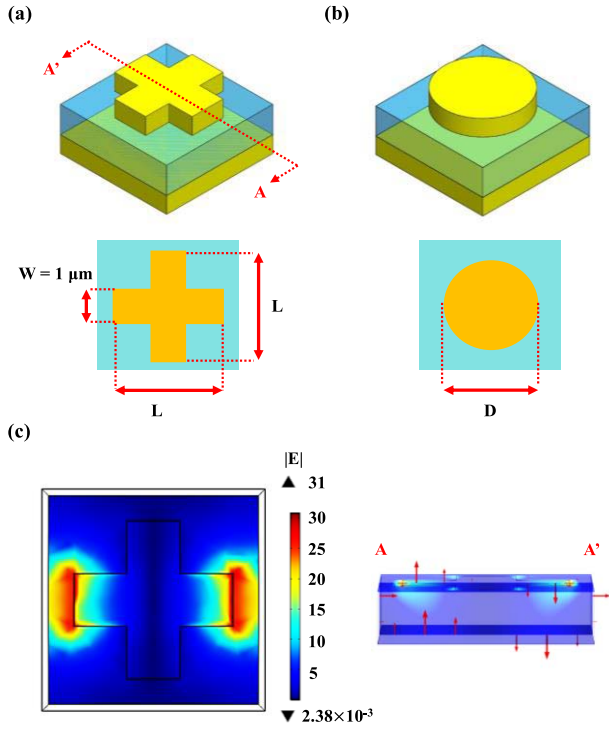

Fig. 3. The designs and simulation results of proposed MIM PMAs, (a) the cross-shape MIM PMA with a characteristic length of L (cross length), (b) the circle-shape MIM PMA with a characteristic length of D (diameter of circle), and (c) the distribution of the electric field intensity (color map) and the induced electric dipoles (arrows) for the cross-shape MIM PMA with L = 2.5μm.

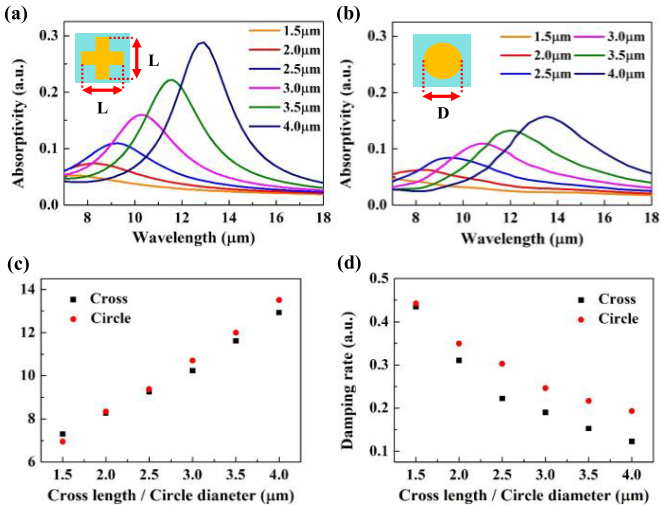

Fig. 4. Simulation results for the uncoupled MIM PMA, (a) the absorption spectra of cross-shape MIM PMA as antenna length L varying from 1.5μm to 4.0μm, (b) the absorption spectra of circle-shape MIM PMA as antenna diameter D varying from 1.5μm to 4.0μm, (c) variation of the absorption peak wavelength λ_{abs} with the characteristic length of antenna (length L and diameter D), and (d) variation of the MIM PMA damping rate with the characteristic length of antenna (length L and diameter D).

well with Eq. (5). Furthermore, the damping rates of MIM PMA determined from the bandwidth of the spectrum are presented in Fig. 4d. The damping rates of both designs decrease with the characteristic length L_c. In conclusion, when the MIM PMA is in the uncoupling regime, the absorption peak wavelength λ_{abs} is sensitive to the characteristic length L_c, and hence any tiny variation (in sub-micrometer scale) in the dimension of antennas may cause the absorption peak wavelength λ_{abs} shifting.

As the absorption peak of MIM PMA approaching the inherent absorption wavelength of SiO_2 film, the MIM PMA will couple with optical phonons in SiO_2 layer [23] to generate two new eigenfrequencies, $\omega_{1,2}$ (note: $\lambda = C/(2\pi\omega)$), where C is the speed of light) [24],

$$\omega_{1,2} = \frac{\omega_{MIM} + \omega_0}{2} \pm \sqrt{V^2 - \left(\frac{\gamma_{MIM} - \gamma_0}{2}\right)^2}, \qquad (6)$$

where ω_{MIM} and ω_0 are respectively the absorption frequencies of MIM PMA and SiO_2, γ_{MIM} and γ_0 are respectively the damping rate of MIM PMA and SiO_2 (coming from optical phonon resonance), and V represents the coupling strength between MIM PMA and SiO_2 dielectric layer. Moreover, the span $\Delta\omega$ between eigenfrequencies ω_1 and ω_2 is,

$$\Delta\omega = \sqrt{4V^2 - (\gamma_{MIM} - \gamma_0)^2}. \qquad (7)$$

According to Eq. (7), the coupling strength V, and damping rates γ_{MIM} and γ_0 are design parameters to determine the span $\Delta\omega$ as well as the absorption wavelength range of proposed MEMS IR sensors. In this study, as limited by the standard CMOS processes, the materials and thicknesses of metal-insulator-metal films are fixed. Thus, the in-plane dimensions of metal antennas are exploited to modulate the damping rate of proposed MIM PMA.

This study also investigates the variation of λ_{abs} with L_c by using the FEM software. In the simulation model, the dispersive refractive index of SiO_2 is specified [17], and the characteristic length L_c of cross-shape and circle-shape metal antennas are respectively ranging from L = 1.5μm to 4.0μm and from D = 1.5μm to 4.0μm, with 0.5μm interval. Simulation results in Fig. 5a-b depict the absorption spectra of coupled MIM PMA with various dimensions of antennas. The peaks between 8μm to 10μm result from the inherent absorption wavelengths of SiO_2 film; the other peaks distributing between 12μm to 19μm indicate the coupled absorption wavelengths between SiO_2 and the MIM PMA. In this case, within the wavelength range of 8 $\sim$ 14μm, the absorption peaks λ_{abs} have no significant changes with the characteristic length L_c. Thus, as compared with the uncoupling case in Fig. 4c, the coupling design could reduce the influence of L_c variation resulting from fabrication processes.

This study employs a peak-fitting method to discern the location of absorption peak wavelengths for Fig. 5. Figure 6a presents a typical example of peak-fitting method for the spectrum of cross-shape antenna with L = 4.0μm. Thus, even for very close peaks in the spectrum (e.g. in the case with smaller characteristic length L_c) can be distinguished through this method. After that, the absorption wavelength spans $\Delta\lambda$ between two coupled peaks for antennas of different shapes and L_c are determined, as shown in Fig. 6b. It indicates that the cross-shape antenna has larger spans $\Delta\lambda$ than the circle-shape antenna with the same L_c. Moreover, as shown

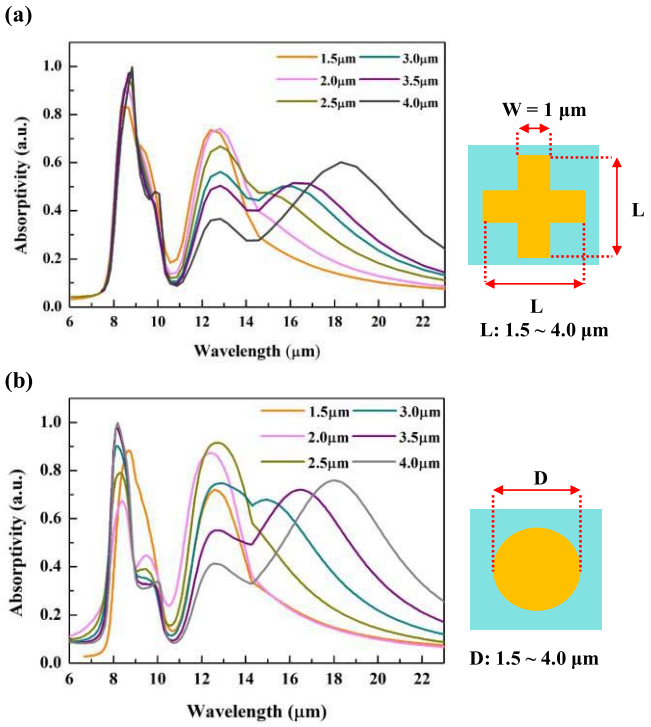

Fig. 5. Simulated absorption spectra for the coupled MIM PMA, (a) the cross-shape antennas as length L varying from 1.5μm to 4.0μm, (b) the circle-shape antennas as diameter D varying from 1.5μm to 4.0μm.

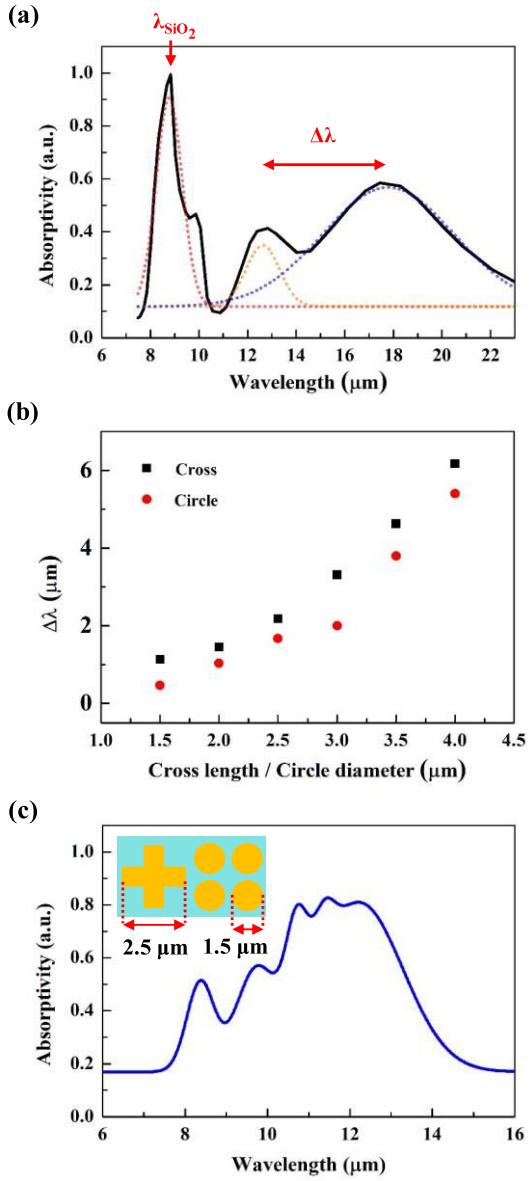

Fig. 6. (a) Distinguishing locations of peak wavelengths by using the peak-fitting method, (b) variation of wavelength span $\Delta\lambda$ for cross-shape and circle-shape antennas of different length L and diameter D, and (c) the absorption spectrum for the proposed MIM design with the combination of cross-shape and circle-shape antennas.

in Fig. 6a, the spectrum exhibits a relatively low absorptivity between two coupled peaks. This is a design concern for broad-band wavelength absorption. In this regard, the damping rate of wavelength absorption peaks can be exploited to modulate the distribution of absorptivity at different wavelengths. As indicated in Fig. 4c-d, for the same characteristic length L_c, the cross-shape and circular-shape antennas have similar absorption wavelength λ_{abs} but different damping rates. Thus, to avoid the low absorptivity between two peaks, this study combines the cross-shape and circle-shape antenna designs to serve as the MIM PMA for the MEMS IR sensor. The cross-shape antenna with L = 2.5μm is selected since its wavelength spans $\Delta\lambda$ is located within 8 $\sim$ 14μm, and the circular-shape with R = 1.5μm is selected since it has a higher damping rate. Simulation in Fig. 6c demonstrates the enhancement of absorption spectrum in the wavelength from 8μm to 14μm after combining antennas of two different shapes. Note that the dimensions and shapes of antennas are not optimized in this study.

III. Fabrication and Results

The fabrication processes of the proposed design are shown in Fig. 7. The integration of the MIM PMA with the MEMS thermoelectric IR sensor was implemented by using the TSMC 0.18μm 1P6M standard CMOS process and the in-house post-CMOS micromachining processes [25], [26]. First of all, as shown in Fig. 7a, the stacking and patterning of each thin film including the poly-Si layer, dielectric layers, and metal layers were prepared by the foundry through the standard CMOS process. Secondly, as presented in Fig. 7b, the metal and tungsten via sacrificial layers were removed by using the H_2SO_4 and H_2O_2 solution through the wet etching process. After that, the serpentine film structure was defined and the window for the etching of Si substrate was also exposed. Thirdly, as illustrated in Fig. 7c, the structure of the IR sensor was released from the Si substrate after the XeF_2 etching process, a gas-phase and isotropic dry etching technology for bulk Si micromachining, and then the thermal isolation was achieved. Note that the poly-Si layer (for thermocouple) was protected by the dielectric films, and would not be etched during the XeF_2 process. Lastly, as displayed in Fig. 7d, the reactive ion etching (RIE) process was conducted to remove the SiO_2 film on top of the metal layers (M5 and M4), so the antennas were completely exposed and the pads were also exposed for wire bonding.

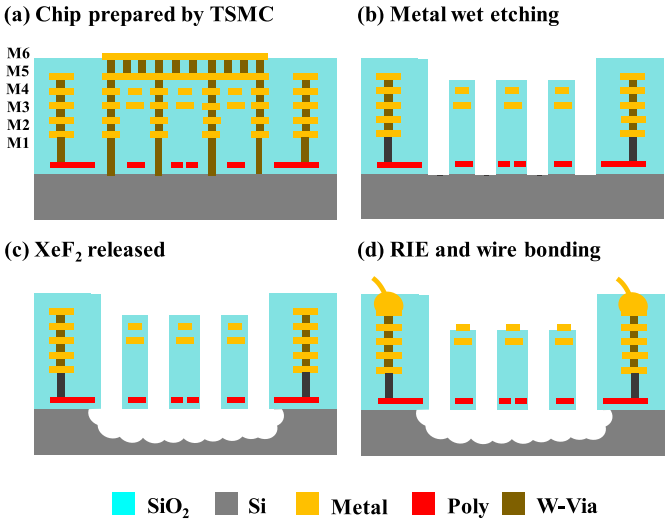

Fig. 7. The fabrication processes of proposed IR sensor with the MIM PMAs, (a) the CMOS chip prepared by the TSMC using standard processes, (b) the metal wet etching by using the H_2SO_4/H_2O_2 solution, (c) the Si substrate etching using the XeF_2 to suspend the MEMS structure for thermal isolation, and (d) the dielectric layer etching using the RIE to expose MIM antennas and bonding pads, and then wire-bonding on pads.

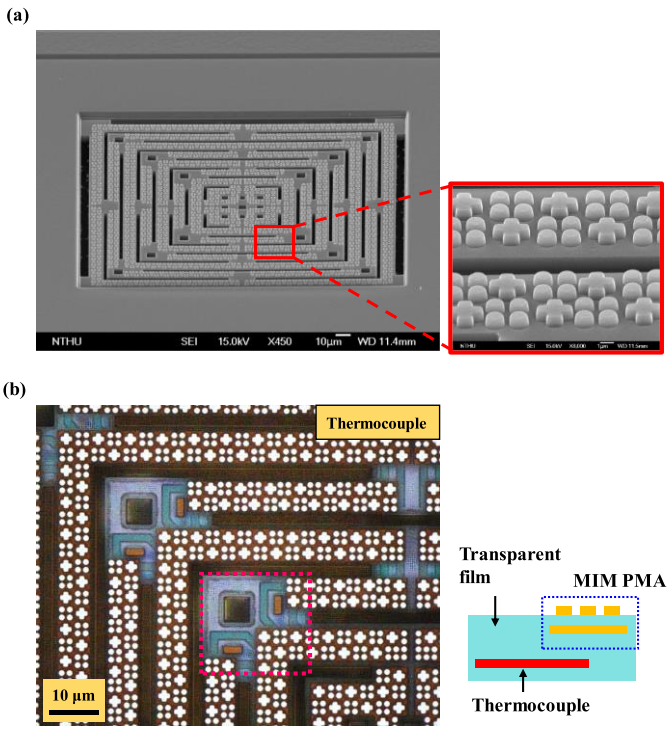

Fig. 8. The micrographs of fabricated devices, (a) the proposed MEMS thermoelectric IR sensor with MIM PMAs on the suspended serpentine structure, and (b) the N-type/P-type poly-Si thermocouples embedded in the transparent dielectric layers and also under MIM PMAs.

The fabricated devices have been observed with the scanning electron microscope (SEM) and the laser confocal microscope. The SEM micrograph in Fig. 8a displays the suspended structure of the IR sensor with in-plane dimensions of $200 \times 200 \mu m^2$. The serpentine structure with MIM PMAs is suspended on the substrate after the XeF_2 etching process. The

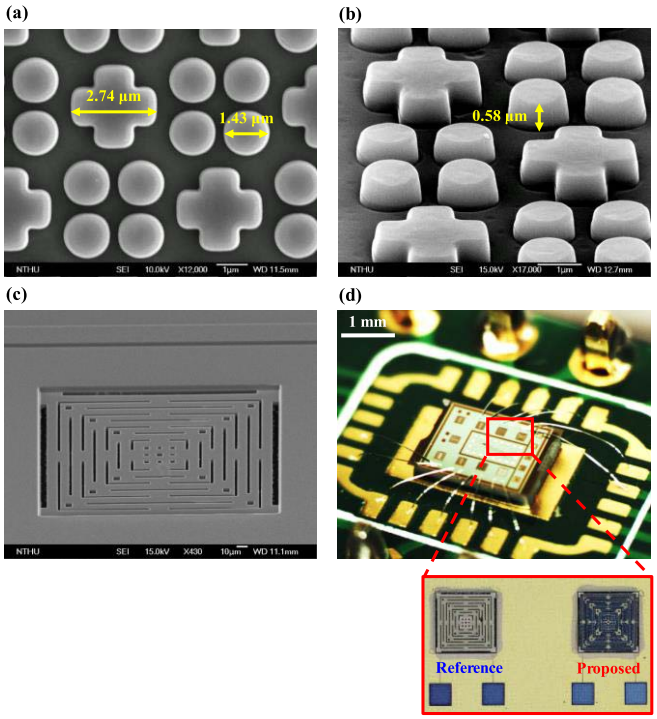

Fig. 9. The micrographs of fabricated devices, (a) the characteristic dimensions of cross-shape and circle-shape MIM antennas, (b) the thickness of MIM antennas (c) the reference design without MIM PMA, (d) the sensing chip mounted and wire-bonded on the PCB as the DUT.

zoom-in micrograph from the laser confocal microscope in Fig. 8b exhibits the cross-shape and circle-shape metal antennas on top of the serpentine suspended structure. Moreover, as marked by the red dashed line, the thermocouples underneath the transparent dielectric layers can be observed. The SEM micrograph in Fig. 9a displays typical metal antennas with planar dimensions of $L = 2.74 \mu m$ (for cross-shape) and $D = 1.43 \mu m$ (for circle-shape). The typical thickness of metal antennas is $0.58 \mu m$, as shown in Fig. 9b. The results indicate the dimensions of fabricated metal antennas are slightly different from the designed ones. The SEM micrograph in Fig. 9c presents the reference IR sensor design with no MIM PMA. Finally, the micrograph in Fig. 9d shows the sensing chip is packaged and wire bonded on the printed circuit board (PCB) as the device under test (DUT). Both of the proposed and reference IR sensors are fabricated on the sensing chip of DUT, so that the test conditions (e.g. the distance between the sensor and the light source, and the field of view) for both sensors are the same to make a fair comparison. Moreover, the surface profiles of the suspended structures for the proposed and reference designs are characterized by using the white light interferometer. As shown in Fig. 10a, the suspended structure of reference design is bent concave downward, and its maximum deformation reaches $0.78 \mu m$. As shown in Fig. 10b, the suspended structure of proposed design is bent concave upward with a maximum deformation of $1.54 \mu m$. The difference of bending curvatures is caused by the additional metal layers for the MIM PMA of the proposed design. Nevertheless, the radius of curvatures for both designs (-9.36mm for the reference design, and 4.82mm for the

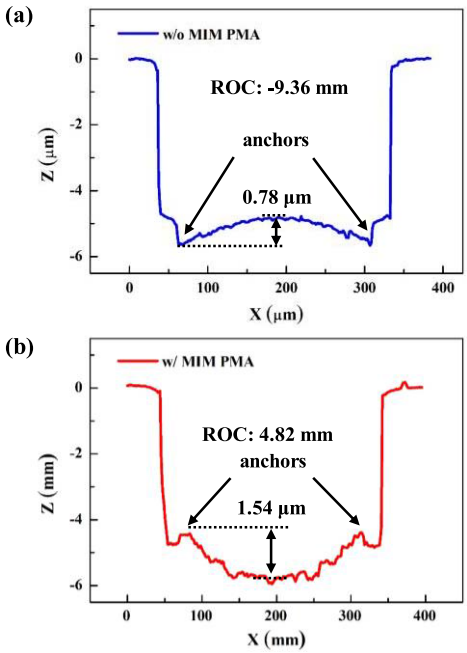

Fig. 10. The surface profiles of IR sensors measured using the white light interferometer, (a) proposed design with the MIM absorber, (b) reference design without the MIM absorber.

TABLE I
THE SPECIFICATIONS AND PERFORMANCES OF PROPOSED AND REFERENCE IR SENSOR DESIGNS IN THIS STUDY

Specifications	w/ MIM absorber	w/o MIM absorber	Units
Active area	200 × 200		μm^2
Resistance	1.39		MΩ
Number of junctions	8		
Responsivity	92.17	76.85	VW^{-1}
NEP	1.63	1.95	nW
Detectivity	6.13	5.13	10^8/W
Response time	20		msec

proposed one) are relatively flat, and hence the influence on the performance of sensor can be ignored.

IV. MEASUREMENTS AND DISCUSSIONS

This study performed various experiments to evaluate the performance of proposed MEMS thermoelectric IR sensors with various MIM PMA designs. In comparison, the reference IR sensor with no MIM PMA is also characterized. Firstly, the absorption spectra of MIM PMAs with three different antenna designs (i.e. (1) cross-shape only, (2) circle-shape only, and (3) combination of cross-shape and circle-shape) are characterized by the Fourier Transform Infrared (FTIR) spectroscopy. After that, the responsivities (output voltage versus incoming radiation power) of proposed and reference IR sensors are determined through the measurement, and then the detectivity and the noise equivalent power (NEP) can be further extracted. Lastly, the response time of the IR sensor is identified through dynamic measurements. Table I summarizes the characteristics and the comparisons of the proposed and the reference MEMS thermoelectric IR sensors.

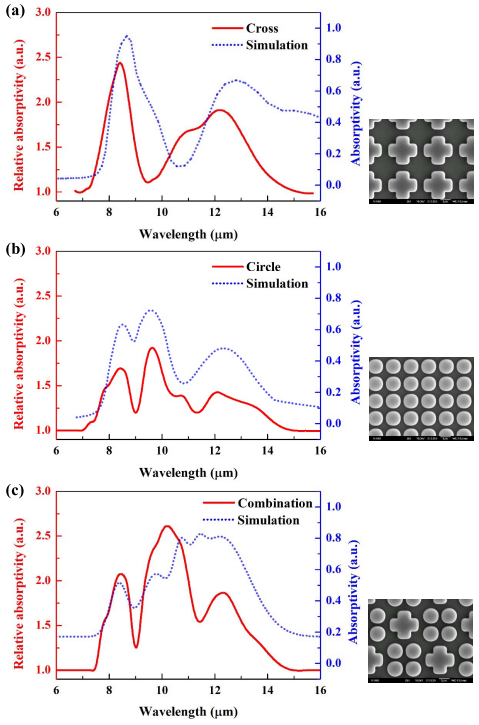

Fig. 11. The measured absorption spectra for MIM PMAs of different antenna designs, (a) the cross-shape antenna, (b) the circle-shape antenna, and (c) combination of the cross-shape and circle-shape antennas.

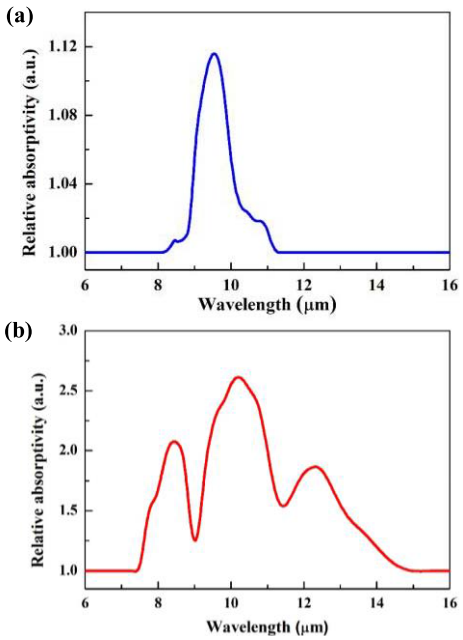

Fig. 12. Measured absorption spectra respectively for, (a) the SiO_2 layer, and (b) the proposed MIM PMA with both cross-shape and circle shape antennas.

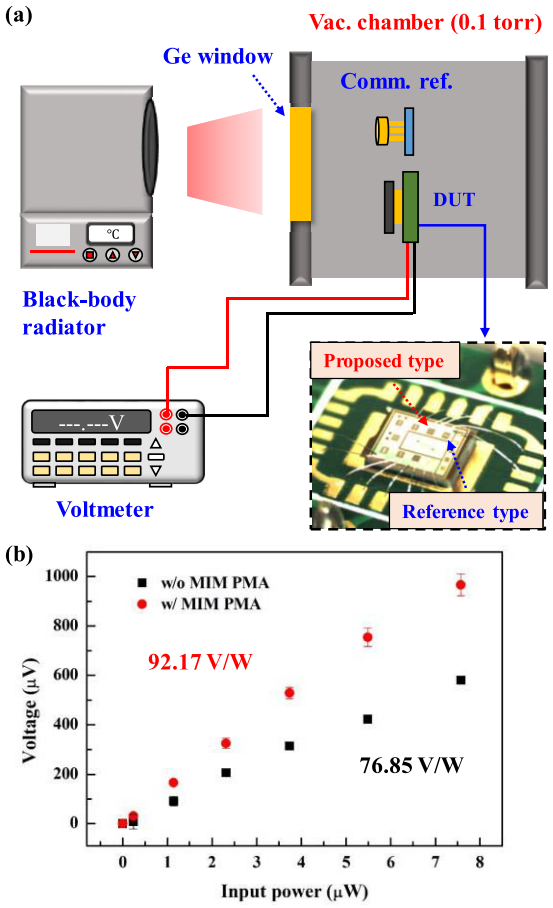

Fig. 13. (a) The experiment setup for the responsivity measurement, and (b) the responsivity of proposed and reference IR sensors determined from the measured output voltage and input power.

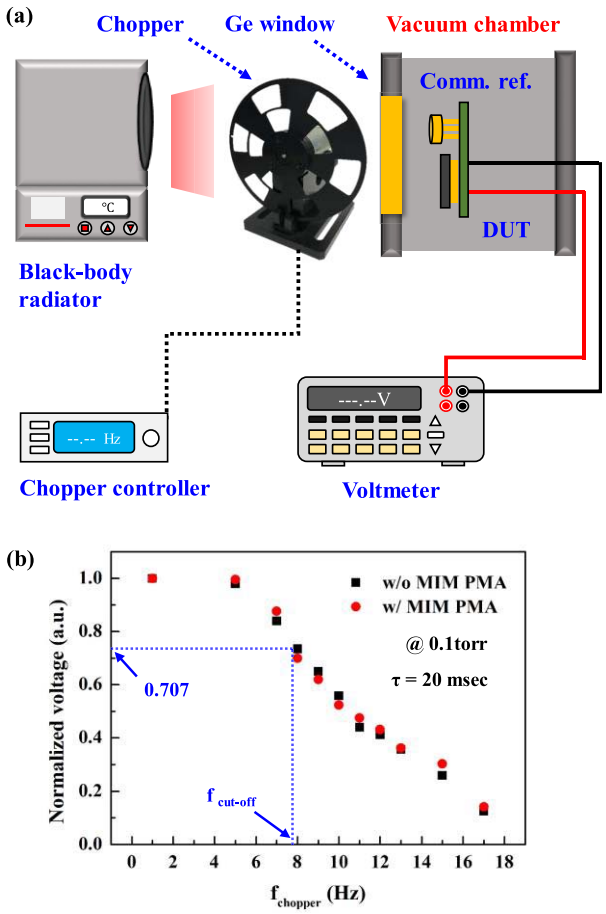

Fig. 14. (a) The experiment setup for the response time measurement, and (b) the response time of proposed and reference IR sensors determined from the normalized output voltage and the cut-off frequency of chopper.

The FTIR measurement results in Fig. 11 show the absorption spectra of MIM PMA respectively for the cross-shape antenna only (Fig. 11a, L: 2.74μm), the circle-shape antenna only (Fig. 11b, D: 1.43μm), and the combination of cross-shape and circle-shape antennas (Fig. 11c, L: 2.74μm and D: 1.43μm). The simulation results are depicted in dashed lines for comparison. The results show that the characteristic lengths L_c of fabricated MIM antennas are slightly different from the designed ones (i.e. L: 2.5μm and D: 1.5μm), yet the measured absorption profiles agree reasonably well with the simulations. This is attributed to the design of proposed MIM PMA in the coupling regime, and hence the variation of dimensions for the fabricated antennas can be tolerated. Furthermore, measured absorption spectra for the reference and proposed IR sensor designs are shown in Fig. 12. Comparing the absorption spectrum of reference design with pure SiO_2 absorber in Fig. 12a, the proposed design with MIM PMA extends the absorption range in the far-infrared region. Note that measurement results are expressed in relative absorptivity (after baseline subtraction) since the FTIR apparatus used in this study can only characterize the MIM PMA qualitatively.

As shown in Fig. 13a, the responsivity measurement setup comprises of a black-body radiator, a vacuum chamber with a germanium window, a voltmeter, a commercial IR sensor, and the DUT. The DUT (including the proposed and reference IR sensors, as displayed in Fig. 9d) is placed in a vacuum chamber with a germanium window as the filter. The germanium window has a high transmission rate in the far-infrared region. In addition, a commercial IR sensor is arranged near the DUT to monitor the incoming radiation power from the black-body radiator. The distance between black-body radiator and DUT is fixed at 13cm and then the field of view is equal to 1. The pressure of vacuum chamber is pumped down to 0.1torr to reduce the influence of heat loss through gas conduction. The output signals from sensors are recorded by the voltmeter. Measurements in Fig. 13b indicate that the responsivities of proposed and reference designs are respectively 92.17V/W and 76.85V/W. The proposed and reference sensors have the same noise level since their thermopile designs are identical. According to the responsivity and noise level, the NEPs for proposed and reference designs are respectively 1.63nW and 1.95nW. Moreover, the detectivities of proposed and reference designs are respectively 6.13×10^8/W and 5.13×10^8/W. The result demonstrates that the proposed design can effectively enhance the performance of MEMS IR sensor in the far-infrared region. As shown in Fig. 14a, the optical chopper with the controller is added to the test setup to measure the response time of MEMS IR sensors. The input radiation signals will be chopped and become square waves with the frequencies determined by the controller. In this

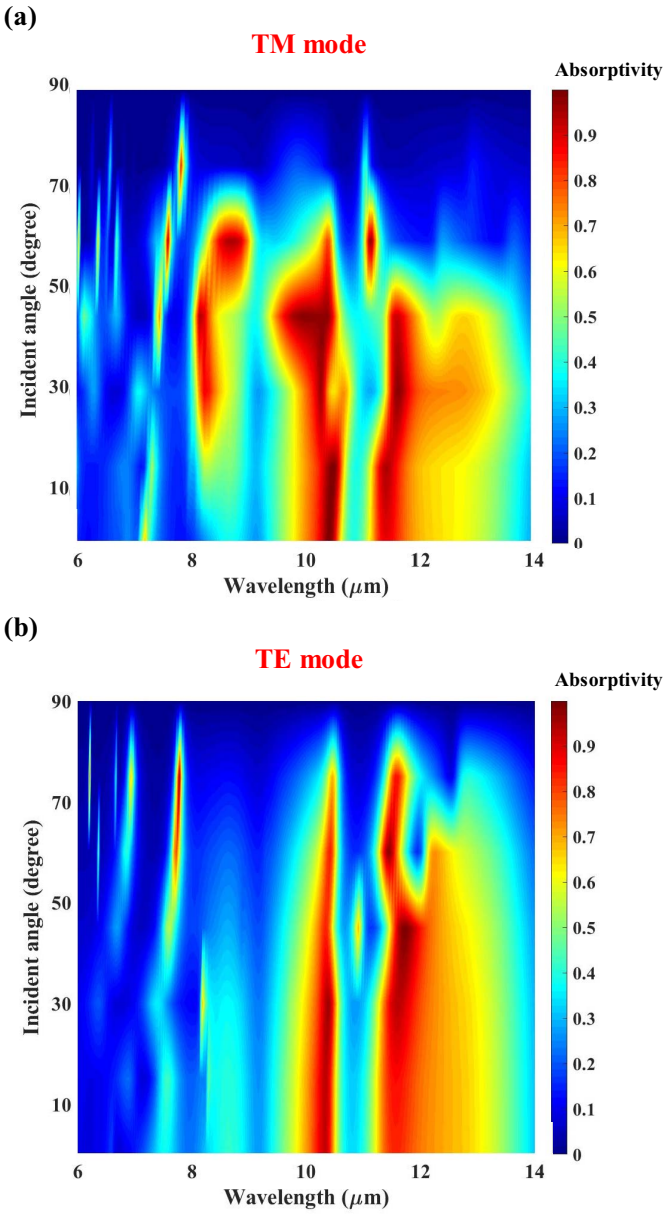

Fig. 15. The simulated absorption spectra for different angles of the incident light, (a) under TM mode, and (b) under TE mode.

measurement, the temperature of black-body radiator is fixed at 180°C and the chopping frequency is varying from 1 to 17Hz. Measurements in Fig. 14b depicts that the normalized voltage signal (root mean square value) from the sensor will drop to 0.707 as the chopper frequency reaches 7.94Hz (named cut-off frequency, $f_{cut-off}$). Thus, the response time τ extracted from the cut-off frequency ($\tau = 1/(2\pi f_{cut-off})$) is 20msec. Note that integrating the MIM PMA only increase little thermal mass, and hence its influence on the response time can be ignored.

V. Conclusion

This study designs and implements MEMS thermoelectric IR sensors with integrated MIM PMAs by using the standard CMOS process platform. The CMOS process offers various advantages for the proposed design, for example, the small linewidth feature could realize antennas with sub-wavelength dimensions and the multi-layer stacking feature could implement the MIM PMAs. This study designs MIM PMAs in the wavelength absorption coupling regime to tolerate the variation of antenna dimensions induced by processes. The cross-shape and circle-shape antennas with different damping rates are designed and integrated on the proposed MIM PMA so that the broad-band wavelength absorption can be achieved. Both the simulation and measurement results demonstrate the feasibility of the proposed MIM PMA design. The absorption spectra measured by FTIR show the capability of MIM PMAs in absorptivity enhancement and absorption range extension. Moreover, measurements also indicate that the responsivity of MEMS thermoelectric IR sensor is increased by 20% (from 76.85V/W to 92.17V/W) after adding the presented MIM PMA. The NEPs for the proposed and reference designs are 1.63nW and 1.95nW respectively. Thus, the proposed sensor also improves the detectivity from 5.1310^8/W to 6.1310^8/W by integrating the MIM PMA. Table I summarizes the comparisons between the proposed and reference designs. In this study, the combination of cross-shape and circle-shape antennas with a specific characteristic length L_c ($L = 2.5\mu m$, $D = 1.5\mu m$) are investigated. The dimensions of antennas can be optimized and other antenna patters can also be proposed to further enhance the performances of the IR sensor. Moreover, the wavelength absorption of the proposed MIM PMA toward different incident angles of light has been investigated through simulations. In the simulation models, the MIM PMA with the combination of cross-shape and circle-shape antennas is respectively illuminated by transverse magnetic (TM) wave and transverse electric (TE) wave. Simulation results in Fig. 15 indicate that the wavelength absorption of presented MIM PMA design has no significant change as the angle of incident light is ranging $0° \sim 50°$. Thus, MIM PMA remains suitable for the absorption of non-normal incident light applications. Further experiment verification regarding this characteristic is still needed.

Acknowledgment

The authors would like to appreciate Taiwan Semiconductor Manufacturing Company (TSMC). They would also like to appreciate the Taiwan Semiconductor Research Institute (TSRI), for the supporting of CMOS chip manufacturing. They also appreciate the Center for Nanotechnology, Materials Science, and Microsystems (CNMM), National Tsing Hua University, for providing the tools in the processes.

References

[1] I. Herrmann *et al.*, "Low-cost approach for integrated long-wavelength infrared sensor arrays," *Procedia Eng.*, vol. 5, pp. 693–696, 2010.
[2] A. Roncaglia, F. Mancarella, and G. C. Cardinali, "CMOS-compatible fabrication of thermopiles with high sensitivity in the 3–5 μm atmospheric window," *Sens. Actuators B, Chem.*, vol. 125, no. 1, pp. 214–223, Jul. 2007.
[3] A. Rogalski, *Infrared Detectors*, 2nd ed. Boca Raton, FL, USA: CRC Press, 2011.
[4] J. Tanaka, H. Imamoto, T. Seki, and M. Oba, "Low power wireless human detector utilizing thermopile infrared array sensor," in *Proc. IEEE SENSORS*, Nov. 2014, pp. 462–465.

[5] D. Xu, E. Jing, B. Xiong, and Y. Wang, "Wafer-level vacuum packaging of micromachined thermoelectric IR sensors," *IEEE Trans. Adv. Packag.*, vol. 33, no. 4, pp. 904–911, Nov. 2010.

[6] M. J. Modarres-Zadeh and R. Abdolvand, "High-responsivity thermoelectric infrared detectors with stand-alone sub-micrometer polysilicon wires," *J. Micromech. Microeng.*, vol. 24, no. 12, Dec. 2014, Art. no. 125013.

[7] S. Ogawa, Y. Takagawa, and M. Kimata, "Broadband polarization-selective uncooled infrared sensors using tapered plasmonic micrograting absorbers," *Sens. Actuators A, Phys.*, vol. 269, pp. 563–568, Jan. 2018.

[8] J. Y. Suen *et al.*, "Multifunctional metamaterial pyroelectric infrared detectors," *Optica*, vol. 4, no. 2, pp. 276–279, Feb. 2017.

[9] Y. Lv, W. Jiang, and W. Ou, "Study of a novel FP microcavity with high infrared absorption," *IEEE Sensors J.*, vol. 5, no. 3, pp. 1756–1760, Mar. 2015.

[10] D. Xu, B. Xiong, and Y. Wang, "Design, fabrication and characterization of a front-etched micromachined thermopile for IR detection," *J. Micromech. Microeng.*, vol. 20, no. 11, Nov. 2010, Art. no. 115004.

[11] T.-W. Shen, K.-C. Chang, C.-M. Sun, and W. Fang, "Performance enhance of CMOS-MEMS thermoelectric infrared sensor by using sensing material and structure design," *J. Micromech. Microeng.*, vol. 29, no. 2, Feb. 2019, Art. no. 025007.

[12] M. Hirota, Y. Nakajima, M. Saito, and M. Uchiyama, "120×90 element thermoelectric infrared focal plane array with precisely patterned Au-black absorber," *Sens. Actuators A, Phys.*, vol. 135, no. 1, pp. 146–151, Mar. 2007.

[13] W. Lang, K. Kuhl, and H. Sandmaier, "Absorbing layers for thermal infrared detectors," in *Proc. Transducers*, San Francisco, CA, USA, Jun. 1991, pp. 635–638.

[14] C. Chen, "Temperature error analysis and parameter extraction of an 8–14-μm thermopile with a wavelength-independent absorber for tympanic thermometer," *IEEE Sensors J.*, vol. 11, no. 10, pp. 2310–2317, Oct. 2011.

[15] Z. Li, S. Butun, and K. Aydin, "Large-area, lithography-free super absorbers and color filters at visible frequencies using ultrathin metallic films," *ACS Photon.*, vol. 2, no. 2, pp. 183–188, Feb. 2015.

[16] J. Hao, J. Wang, X. Liu, W. J. Padilla, L. Zhou, and M. Qiu, "High performance optical absorber based on a plasmonic metamaterial," *Appl. Phys. Lett.*, vol. 96, no. 25, Jun. 2010, Art. no. 251104.

[17] J. Kischkat *et al.*, "Mid-infrared optical properties of thin films of aluminum oxide, titanium dioxide, silicon dioxide, aluminum nitride, and silicon nitride," *Appl. Opt.*, vol. 51, no. 28, pp. 6789–6798, 2012.

[18] P.-S. Lin, T.-W. Shen, K.-C. Chang, and W. Fang, "Monolithic integration of plasmonic meta-material absorber with CMOS-MEMs infrared sensor for responsivity enhancement and human detection application," in *Proc. IEEE 33rd Int. Conf. Micro Electro Mech. Syst. (MEMS)*, Vancouver, BC, Canada, Jan. 2020, pp. 157–160.

[19] S.-K. Yeh, J.-H. Lee, and W. Fang, "Development of the backside loading inductive tactile force sensor using the flip-chip bonding of CMOS sensing chip," *IEEE Sensors J.*, vol. 20, no. 6, pp. 2868–2876, Mar. 2020.

[20] H. Budzier and G. Gerlach, *Thermal Infrared Sensors: Theory, Optimization and Practice*. Hoboken, NJ, USA: Wiley, 2011.

[21] K.-C. Chang, Y.-C. Lee, C.-M. Sun, and W. Fang, "Novel absorber membrane and thermocouple designs for CMOS-MEMS thermoelectric infrared sensor," in *Proc. IEEE 30th Int. Conf. Micro Electro Mech. Syst. (MEMS)*, Las Vegas, NV, USA, Jan. 2017, pp. 1228–1231.

[22] J. Kim *et al.*, "Role of epsilon-near-zero substrates in the optical response of plasmonic antennas," *Optica*, vol. 3, no. 3, p. 339, Mar. 2016.

[23] D. J. Shelton *et al.*, "Strong coupling between nanoscale metamaterials and phonons," *Nano Lett.*, vol. 11, no. 5, pp. 2104–2108, May 2011.

[24] A. Kavokin, J. J. Baumberg, G. Malpuech, and F. P. Laussy, *Microcavities*. Oxford, U.K.: Oxford Univ. Press, 2007.

[25] D. Xu, B. Xiong, G. Wu, Y. Ma, and Y. Wang, "Uncooled thermoelectric infrared sensor with advanced micromachining," *IEEE Sensors J.*, vol. 12, no. 6, pp. 2014–2023, Jun. 2012.

[26] M.-H. Tsai, C.-M. Sun, Y.-C. Liu, C. Wang, and W. Fang, "Design and application of a metal wet-etching post-process for the improvement of CMOS-MEMS capacitive sensors," *J. Micromech. Microeng.*, vol. 19, no. 10, Sep. 2009, Art. no. 105017.

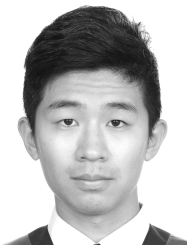

Pen-Sheng Lin was born in Taipei, Taiwan. He received the B.S. degree from the Department of Physics, National Tsing Hua University, Taiwan, where he is currently pursuing the M.S. degree with the Department of Power Mechanical Engineering. His research interests include the design and implementation of thermoelectric IR sensors, metamaterials, light-matter interaction, and the implementation of CMOS-MEMS sensors.

Ting-Wei Shen was born in Taichung, Taiwan. He received the B.S. degree from the Department of Power Mechanical Engineering, National Tsing Hua University, Taiwan, in 2016, and the M.S. degree from the Institute of Nano-Engineering and MicroSystems, National Tsing Hua University in 2018. His research interests include the design and implementation of thermoelectric IR sensors and the implementation of CMOS-MEMS sensors.

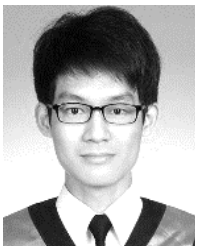

Kai-Chieh Chan was born in Taipei, Taiwan. He received the B.S. and M.S. degrees from the Department of Power Mechanical Engineering, National Tsing Hua University, Taiwan, in 2014 and 2016, respectively. His research interest includes the design and implementation of thermoelectric IR sensors, micromirrors, and MEMS environment sensors.

Weileun Fang (Fellow, IEEE) was born in Taipei, Taiwan. He received the Ph.D. degree from Carnegie Mellon University in 1995. His doctoral research focused on the determination of the mechanical properties of thin films using micromachined structures. In 1995, he worked as a Postdoctoral Researcher at the Synchrotron Radiation Research Center, Taiwan. He joined the Department of Power Mechanical Engineering, National Tsing Hua University, Taiwan, in 1996, where he is currently a Chair Professor as well as a Faculty Member of the NEMS Institute. In 1999, he was a Visiting Associate with the California Institute of Technology, along with Prof. Y.-C. Tai. His research interests include MEMS with an emphasis on microfabrication/packaging technologies, CMOS-MEMS, CNT MEMS, micro-optical systems, microsensors and actuators, and the characterization of thin-film mechanical properties. He was elevated to IEEE Fellow in 2015 as a recognition for his contribution in the MEMS area. He has a close collaboration with MEMS industries and is currently the VP of the MEMS and Sensors Committee of SEMI Taiwan. He served as a member of the International Steering Committee (ISC) of Transducers from 2009 to 2017 and the ISC Chair from 2017 to 2019. He also served as the General Chair of the transducers conference in 2017. He was the TPC of the IEEE MEMS and EPC of Transducers for many years and the Program Chair of the IEEE Sensors Conference in 2012. He served as the Chief Delegate of the World Micromachine Summit (MMS), Taiwan, from 2008 to 2012, and the General Chair of MMS in 2012. He is currently the Chief Editor of the JMM, an Associate Editor of the IEEE SENSORS JOURNAL, and the Board Member of the IEEE TRANSACTIONS ON DEVICE AND MATERIALS RELIABILITY.